Supplementary Information (SI) for Nanoscale.

Supporting Information for "Fast and accurate characterization of bioconjugated particles and solvent properties by a general nonlinear analytical relation for the AC magnetic hysteresis area"

Pablo Palacios-Alonso,[†] Mohamed. M. Shams,[‡] Sedef Ozel-Okcu,[‡] Elena Sanz-de Diego,[‡] F.J. Teran,[‡] and Rafael Delgado-Buscalioni[*,†]

†*Dpto. Física Teórica de la Materia Condensada, Universidad Autónoma de Madrid, Madrid, 28049, Spain*

‡*iMdea Nanociencia, Campus Universitario de Cantoblanco, 28049 Madrid, Spain*

¶*Nanobiotecnología (iMdea-Nanociencia), Unidad Asociada al Centro Nacional de Biotecnología (CSIC), 28049 Madrid, Spain*

§*Condensed Matter Institute, IFIMAC, Madrid, 28049, Spain*

‖*Dpto. Física Teórica de la Materia Condensada, Universidad Autónoma de Madrid, 28049 Madrid, Spain. Institute of Condended Matter (IFIMAC).*

E-mail: rafael.delgado@uam.es

Supporting information

Sensitivity of the Area to Changes in Size

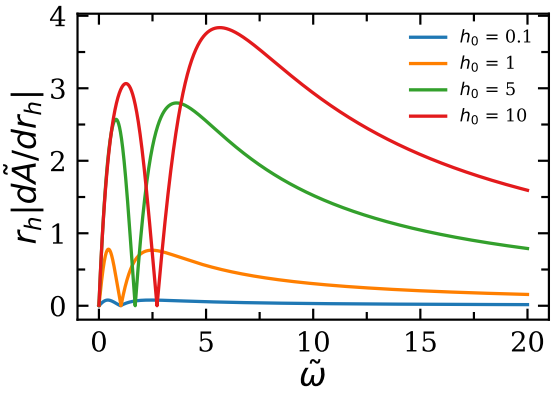

Figure S1: Absolute value of the derivative of the dimensionless area with respect to the hydrodynamic radius as a function of $\tilde{\omega}$ for different values of h_0.

Figure S1 illustrates the absolute value of the derivative of the dimensionless area with respect to the hydrodynamic radius, expressed as:

$$\frac{d\tilde{A}}{dr_h} = \frac{d\tilde{A}}{d\tilde{\omega}}\frac{d\tilde{\omega}}{dr_h} = 3r_h\tilde{\omega}\frac{d\tilde{A}}{d\tilde{\omega}}, \tag{1}$$

as a function of $\tilde{\omega}$ for different values of h_0. The results indicate that higher values of h_0 lead to greater maximum values of the derivative. This observation suggests that biosensing applications based on detecting changes in the hydrodynamic size of MNPs, resulting from their interaction with molecules, will exhibit increased sensitivity when stronger AMF amplitudes are employed.

Comparison Between Cycles Calculated Using the LRT and Those Obtained by Numerically Solving the FP Equation

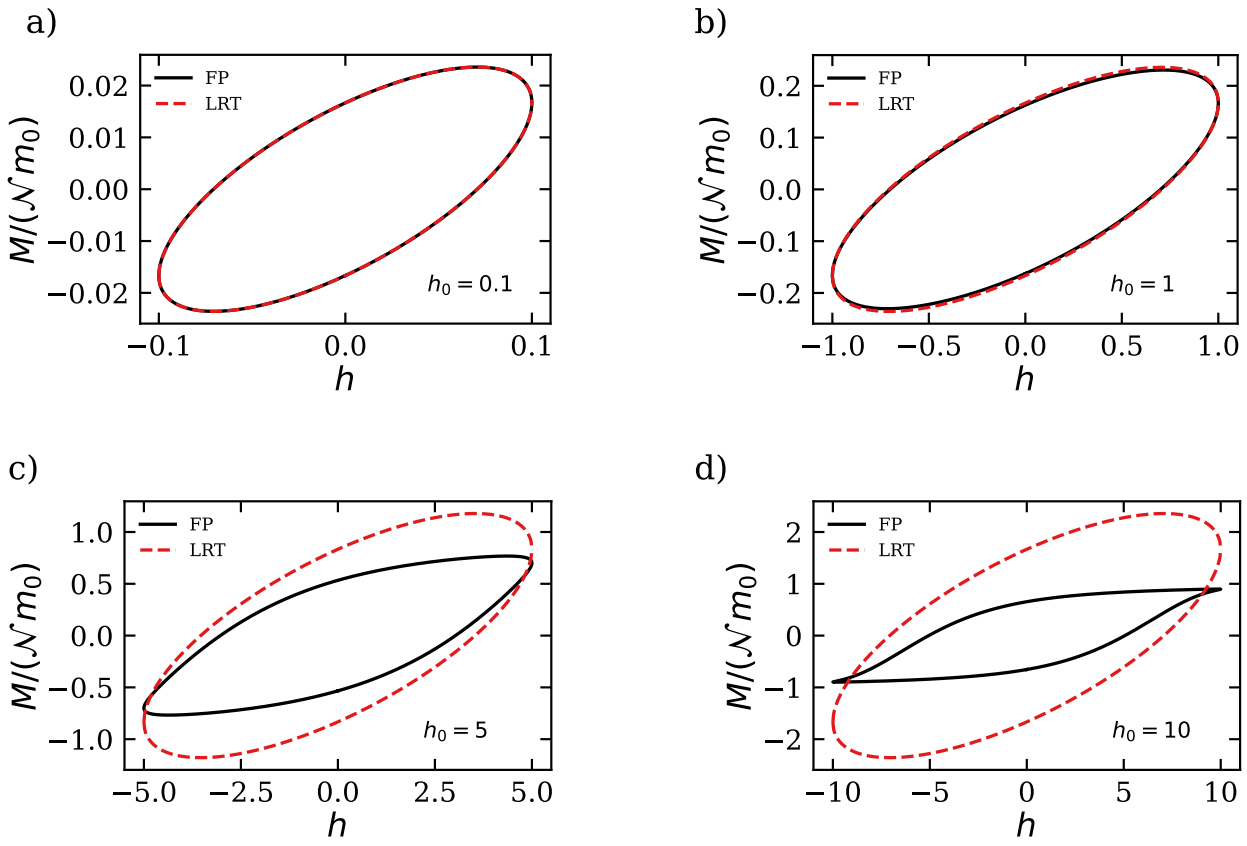

Figure S2: Comparison between the cycles computed using the LRT (red dashed lines) and those obtained by solving the FP equation (black continuous lines) for different values of h_0 when $\tilde{\omega} = 1$.

In this section, we compare the cycles calculated using the LRT with those obtained by numerically solving the FP equation. When $h_0 \lesssim 1$, both methods yield similar cycles. However, as h_0 increases, the magnetic moment of the cycles calculated using the FP equation begins to saturate. This occurs because the normalized magnetization, defined as the magnetization divided by the maximum magnetization achievable by the system ($\mathcal{N}m_0$), cannot exceed 1. Since saturation is a nonlinear effect, it is not captured by the LRT, which causes the system's magnetization to exceed the maximum physical value. As a result, the area calculated using the LRT continues to increase with h_0, diverging from the behavior

predicted by the FP equation.

Dependence of the Hysteresis Area on $\tilde{\omega}$ and h_0 in the Low-Frequency Regime

In this section, we analyze in detail how the area of the cycles varies with $\tilde{\omega}$ in the low-frequency regime ($\tilde{\omega} \ll 1$). Figure S3a shows the area as a function of $\tilde{\omega}$ for various values of h_0, calculated numerically (dots) and compared with the predictions of the LRT. For sufficiently low values of $\tilde{\omega}$, the area increases linearly with the dimensionless frequency, following $\tilde{A} = \alpha(h_0)\tilde{\omega}$, as predicted by the LRT. However, while the LRT predicts that the slope of the line is $\alpha(h_0) = \pi h_0/3$, this prediction becomes invalid when $h_0 \gtrapprox 1$, as the actual slope is lower than the LRT.

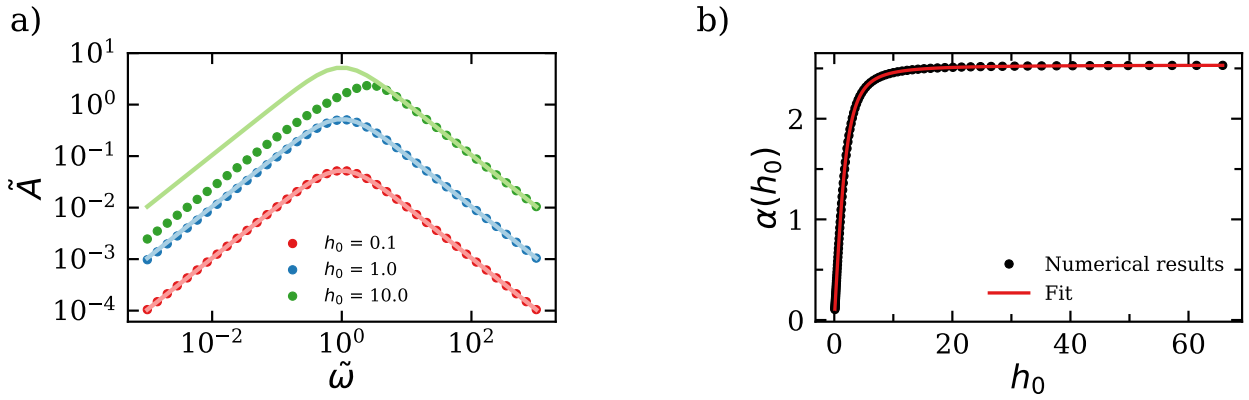

Figure S3: a) Dependence of the area on $\tilde{\omega}$, calculated by numerically solving the FP equation (dots), compared with the LRT prediction. b) Dependence of the function $\alpha(h_0)$ on h_0, calculated from the numerical results (dots) and fitted to equation 2 (line).

To approximate $\alpha(h_0)$ for any value of h_0, we calculated the slope of the line for a range of h_0 values. The results are shown in Figure S3b. When h_0 is small, the slope increases linearly with h_0, following $\alpha(h_0) = \pi h_0/3$. However, for large values of h_0, the slope saturates at 2.532. To model this behavior, we considered a family of functions of the form:

$$\alpha(h_0) = \frac{\pi}{3} \cdot \frac{h_0}{(1 + a h_0^k)^{1/k}}, \tag{2}$$

where a and k are constants. By fitting the numerical results, we determined that $k = 2.05$ and $a = 0.16$ provide an accurate representation of $\alpha(h_0)$, as shown by the red line in Figure S3b.

In conclusion,

$$\tilde{A}(\tilde{\omega} \ll 1, h_0) = \frac{\pi h_0 \tilde{\omega}}{3\left(1 + 0.16 h_0^{2.05}\right)^{\frac{1}{2.05}}} \tag{3}$$

Dependence of the Hysteresis Area on h_0 in the High-Field Regime

In this section, we analyze the variation of the hysteresis area with the dimensionless parameters in the high-field regime ($h_0 \gg 1$). As shown in Figure 3e, in this regime, the area of the cycles approaches zero, following a power law of the form $\tilde{A}(\tilde{\omega}, h_0 \gg 1) = g(\tilde{\omega}) h_0^{-0.45}$. Similar to the approach used in the previous section, we calculated $g(\tilde{\omega})$ for various values of $\tilde{\omega}$ and plotted the results in Figure S4. The results show that $g(\tilde{\omega}) = 8\tilde{\omega}^{0.55}$.

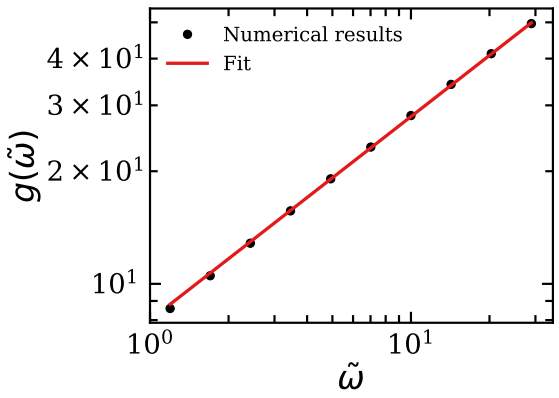

Figure S4: Dependence of the function $g(\tilde{\omega})$ on $\tilde{\omega}$, calculated from the numerical results (dots) and fitted to a power law (line).

Using this result we can conclude,

$$\tilde{A}(\tilde{\omega}, h_0 \gg 1) = \frac{8\tilde{\omega}^{0.55}}{h_0^{0.45}} \tag{4}$$

Derivation of the Universal Relation for the Area

In this section, we consolidate the findings from the analysis of the hysteresis area across different regimes into a single universal relation. To this end, we define a function $\tilde{A}_0(\tilde{\omega}; h_0)$, which exhibits a single maximum and asymptotic power-law decay as $\tilde{\omega} \to 0$ and $\tilde{\omega} \to \infty$. The function $\tilde{A}_0$ explicitly depends on the variable $\tilde{\omega}$ and five parameters, which are themselves functions of h_0. These parameters determine the position and magnitude of the maximum of $\tilde{A}_0$, as well as the power-law exponents governing its asymptotic decay for $\tilde{\omega}$ deviating from $\tilde{\omega}_{\max}$, both for $\tilde{\omega} < \tilde{\omega}_{\max}$ and $\tilde{\omega} > \tilde{\omega}_{\max}$. A function $\tilde{A}_0(\tilde{\omega}; h_0)$ satisfying these conditions is given by

$$\tilde{A}_0(\tilde{\omega}; h_0) = \frac{(\tilde{\omega}/\tilde{\omega}_{\max})^{p_0}}{(c_2 + c_1(\tilde{\omega}/\tilde{\omega}_{\max})^{p_2})^{p_1}}. \tag{5}$$

If $p_1 \cdot p_2 > p_0$, this function tends to 0 as $\tilde{\omega} \to \infty$, as

$$\tilde{A}_0(\tilde{\omega} \gg 1; h_0) = \left(\frac{1}{c_1}\right)^{p_1} \cdot \left(\frac{\tilde{\omega}}{\tilde{\omega}_{\max}}\right)^{p_0 - p_1 \cdot p_2}. \tag{6}$$

According to the LRT, in this limit, the function must approach zero as $\tilde{A}_{LRT}(\tilde{\omega} \gg 1, h_0) = \frac{\pi h_0}{3\tilde{\omega}}$, which imposes two constraints on the parameters:

$$p_0 - p_1 \cdot p_2 = -1 \tag{7}$$

$$\left(\frac{1}{c_1}\right)^{p_1} = \frac{\pi h_0}{3\tilde{\omega}} \tag{8}$$

Furthermore, this function has a maximum at

$$\tilde{\omega} = \tilde{\omega}_{\max} \left(\frac{p_0 c_2}{c_1(p_1 p_2 - p_0)}\right)^{\frac{1}{p_2}} \tag{9}$$

For the maximum to occur at $\tilde{\omega} = \tilde{\omega}_{\max}$, an additional condition on the parameters must be imposed. Combined with Equation 7, this condition can be expressed as:

$$\frac{p_0 \cdot c_2}{c_1} = 1 \tag{10}$$

Furthermore, the maximum value of the area for a given value of h_0 (Equation 6 in the main text) provides another constraint, expressed as:

$$\tilde{A}_{\max} = \left(\frac{1}{c_1 + c_2}\right)^{p_1} \tag{11}$$

Up to this point, we have derived four equations for the five parameters. To fully determine all the parameters, an additional condition must be imposed. This condition arises from the power-law behavior that governs how the area approaches its maximum: in the linear regime, when $\tilde{\omega} < \tilde{\omega}_{\max}$, the area grows as $\tilde{A} \propto \tilde{\omega}$. However, for $h_0 \gg 1$, it has been shown that $\tilde{A} \propto \tilde{\omega}^{0.55}$ (see Equation 4 in the main text). To reproduce this behavior, we postulate that p_0 is a function of h_0 given by:

$$p_0 = 1 - 0.45 \exp[-n_1 h_0^{-n_2}] \tag{12}$$

such that when $h_0 \to 0$, $p_0 \to 1$, and when $h_0 \to \infty$, $p_0 \to 0.55$. Here, n_1 and n_2 are constants to be fitted later. Using all the conditions mentioned above, it is now possible to express all the parameters as functions of known values and p_0:

$$\begin{aligned}
p_1 &= \log\left(\frac{\pi h_0}{3\tilde{\omega}_{\max}}\right) \cdot \left[\log\left(\frac{p_0 + 1}{p_0}\right)\right]^{-1} && (13)\\
p_2 &= \frac{p_0 + 1}{p_1} && (14)\\
c_1 &= \frac{p_0}{p_1 \cdot p_2} \cdot \tilde{A}_{\max}^{-\frac{1}{p_1}} && (15)\\
c_2 &= \frac{c_1}{p_0} && (16)\\
& && (17)
\end{aligned}$$

Note that when $h_0 \ll 1$, the following approximations hold: $p_0 \approx 1$, $\tilde{\omega}_{\max} \approx 1$, $\tilde{A}_{\max} \approx \frac{\pi h_0}{6}$, and consequently, $p_1 = 1$, $p_2 = 2$, and $c_1 = c_2 = \frac{3}{\pi h_0}$. Under these conditions, the LRT equation is recovered. Furthermore, by construction, the position and value of the maximum for any value of h_0 are correctly reproduced, as well as the behavior for large values of $\tilde{\omega}$. However, the behavior when $\tilde{\omega} \to 0$ and $h_0 \geq 1$ is not accurately captured, as shown in the main text: the area should grow linearly when $\tilde{\omega}$ is very small and, for larger values of $\tilde{\omega}$, grow as $\tilde{\omega}^{0.55}$. To account for this behavior, we replace the term $\left(\frac{\tilde{\omega}}{\tilde{\omega}_{\max}}\right)^{p_0}$ with the following adjusted term:

$$\text{Num} = \frac{\tilde{\omega}/\tilde{\omega}_{\max}}{(c_3 + (\tilde{\omega}/\tilde{\omega}_{\max})^{p_3})^{p_4}}. \tag{18}$$

Here, p_3 and p_4 must satisfy the condition:

$$1 - p_3 \cdot p_4 = p_0 \tag{19}$$

to ensure that the behavior at intermediate values of $\tilde{\omega}$ is preserved.Additionally, for the area in the low-frequency regime to satisfy Equation 3, it is necessary that c_3 satisfies:

$$c_3 = \left(\frac{1}{\alpha \tilde{\omega}_{\max} c_2^{p_1}}\right)^{\frac{1}{p_4}} \tag{20}$$

With this new term, we have introduced three additional parameters but only two conditions to determine them, leaving one free parameter ($p_3 = n_3$), which will be adjusted once the final form of the equation is established. At this stage, the equation for the area can be written as:

$$\tilde{A}_1 = \frac{\tilde{\omega}/\tilde{\omega}_{\max}}{[c_3 + (\tilde{\omega}/\tilde{\omega}_{\max})^{p_3}]^{p_4} \cdot [c_2 + c_1(\tilde{\omega}/\tilde{\omega}_{\max})^{p_2}]^{p_1}} \tag{21}$$

Finally, we introduce an additional correction to ensure that, as $h_0 \to \infty$, the area approaches zero in accordance with Equation 4 of the main text. To achieve this, we define

a new function, c_4, which depends on h_0 and $\tilde{\omega}$, and include it as a multiplicative factor for $(\tilde{\omega}/\tilde{\omega}_{\max})^{p_3}$ in the first term of the denominator. This results in the final expression:

$$\tilde{A} = \frac{\tilde{\omega}/\tilde{\omega}_{\max}}{[c_2 + c_1(\tilde{\omega}/\tilde{\omega}_{\max})^{p_2}]^{p_1} \cdot [c_3 + (1 + c_4)(\tilde{\omega}/\tilde{\omega}_{\max})^{p_3}]^{p_4}} \tag{22}$$

To preserve the limits already adjusted, c_4 must approach zero as $\tilde{\omega} \to \infty$ and as $h_0 \to 0$. Additionally, it must tend to zero following a power-law behavior as $h_0 \to \infty$. To satisfy these conditions, we propose the following function:

$$c_4 = \frac{n_4}{h_0^{n_5}}, \exp\left[-\left(n_6\tilde{\omega}^{n_7} + n_8 h_0^{-n_9}\right)\right] \tag{23}$$

In this way, we have now established the final form of the phenomenological equation for the area. The remaining step is to determine the values of the coefficients n_i. To achieve this, we employ the same Monte Carlo (MC) algorithm described in the next section. In this case, the objective is to minimize the average relative error between the area values obtained using the FPE and those predicted by Equation 22 for a given combination of n_i values. This procedure yields the following results: $n_1 = 8.5$, $n_2 = 1.75$, $n_3 = 1.8$, $n_4 = 1600$, $n_5 = 0.5$, $n_6 = 6.33$, $n_7 = 0.18$, $n_8 = 11$, $n_9 = 1$.

Parallel Tempering Algorithm

In this section, we will provide a detailed description of the parallel tempering algorithm employed.

The goal of the algorithm is to find a set of parameters (Λ) that optimally fits an equation to a set of experimental data. These data are obtained by varying one or more known experimental parameters (ξ), and the equation aims to reproduce the experimental measurements using both the known parameters ξ and the unknown parameters Λ. The algorithm finds the vector Λ that minimizes an error function $\mathcal{C}(\Lambda)$, which measures how well the equation fits the experimental data.

In the system we are studying, the known parameters are $\xi = \{f, H_0\}$, while the parameters we wish to determine are $\Lambda = \{r_h, \sigma_c, M_s, \dots\}$, along with any other experimental values that affect the area and remain unknown. The error function used in this work is:

$$\mathcal{C}(\Lambda) = \sum_{i=1}^{N_{ex}} \frac{\left|A(\Lambda, \xi^{(i)}) - A_{exp}(\xi^{(i)})\right|}{A_{exp}(\xi^{(i)})} \tag{24}$$

Operation of the Algorithm

The algorithm starts by creating several "replicas" of the system, each with an initial set of parameters Λ^j and an assigned Monte Carlo temperature (T^j_{MC}). The temperature controls the degree of exploration for each replica. Replicas with higher temperatures tend to make larger changes in the parameters, allowing them to explore the solution space more broadly and move between different local minima. In contrast, replicas with lower temperatures make smaller adjustments, refining the search in regions closer to a local minimum.

Within each replica, a Monte Carlo process is used to adjust the parameters Λ^j. In each step, the algorithm randomly selects one of the parameters Λ^j_i and modifies it by an amount $\Delta\Lambda^j_i = w\Lambda^j_i$, where w is a random number generated uniformly between $-\varepsilon$ and ε. The value of ε is a computational parameter that controls the size of the adjustments in each iteration: if it is too small, the algorithm progresses slowly, leading to potentially slow convergence. On the other hand, if ε is too large, the changes in the parameters can be too abrupt, making it difficult to find the minimum. In this work, $\varepsilon = 0.05$ has been used.

Once the parameter Λ^j_i has been modified, the value of the error function $\mathcal{C}(\Lambda^j_i)$ is recalculated with the new parameters. If the error decreases, the change in the parameters is automatically accepted. If the error increases, the change may still be accepted or rejected, based on a probability that depends on the temperature of the replica. This acceptance probability is defined by the equation:

$$P_{acc} = \exp\left[-\frac{\mathcal{C}(\Lambda_{new}) - \mathcal{C}(\Lambda_{old})}{T_{MC}}\right] \tag{25}$$

where Λ^j_{new} is the new set of parameters, and Λ^j_{old} is the previous set of parameters. At higher temperatures, the probability of accepting even worse solutions is greater, which helps avoid getting trapped in local minima. At lower temperatures, only solutions that improve or maintain the error are accepted, further refining the final adjustment.

This process is repeated iteratively and in parallel for each temperature, and every N_{swap} steps, an attempt is made to exchange parameters Λ^j between replicas at different temperatures. To do this, a temperature T^j_{MC} is randomly selected, and an attempt is made to exchange the parameters between replicas at temperatures T^j_{MC} and T^{j+1}_{MC} with a probability given by:

$$P_{swap} = \min\left(1, \exp\left[(\beta_j - \beta_{j+1})(\mathcal{C}(\Lambda^{best}_j) - \mathcal{C}(\Lambda^{best}_{j+1}))\right]\right) \tag{26}$$

where $\beta_j = \frac{1}{T^j_{MC}}$ and Λ^{best}_j is the set of parameters corresponding to temperature j that produced the lowest error. The process then continues by attempting to exchange parameters between replicas at temperatures T^{j+2}_{MC} and T^{j+3}_{MC}, and so on. When $j + n$ exceeds the total number of temperatures, the process resumes from the first temperature (j=0), ensuring that all replicas are evaluated cyclically. This allows for faster exploration of the parameter space than would be possible with a fixed temperature adjustment. Once the parameter swaps between all temperatures have been attempted, the fitting algorithm continues from the parameters Λ^{best}_j.

This iterative process runs until the number of steps without achieving a reduction in the error reaches a given threshold (N_{end}), or until a predefined maximum number of steps is reached (N_{max}).

In this work, we have used $N_{end} = 1000$, $N_{max} = 100000$, and $N_{swap} = 100$.

Effect of the number of measures in the quality of the fit

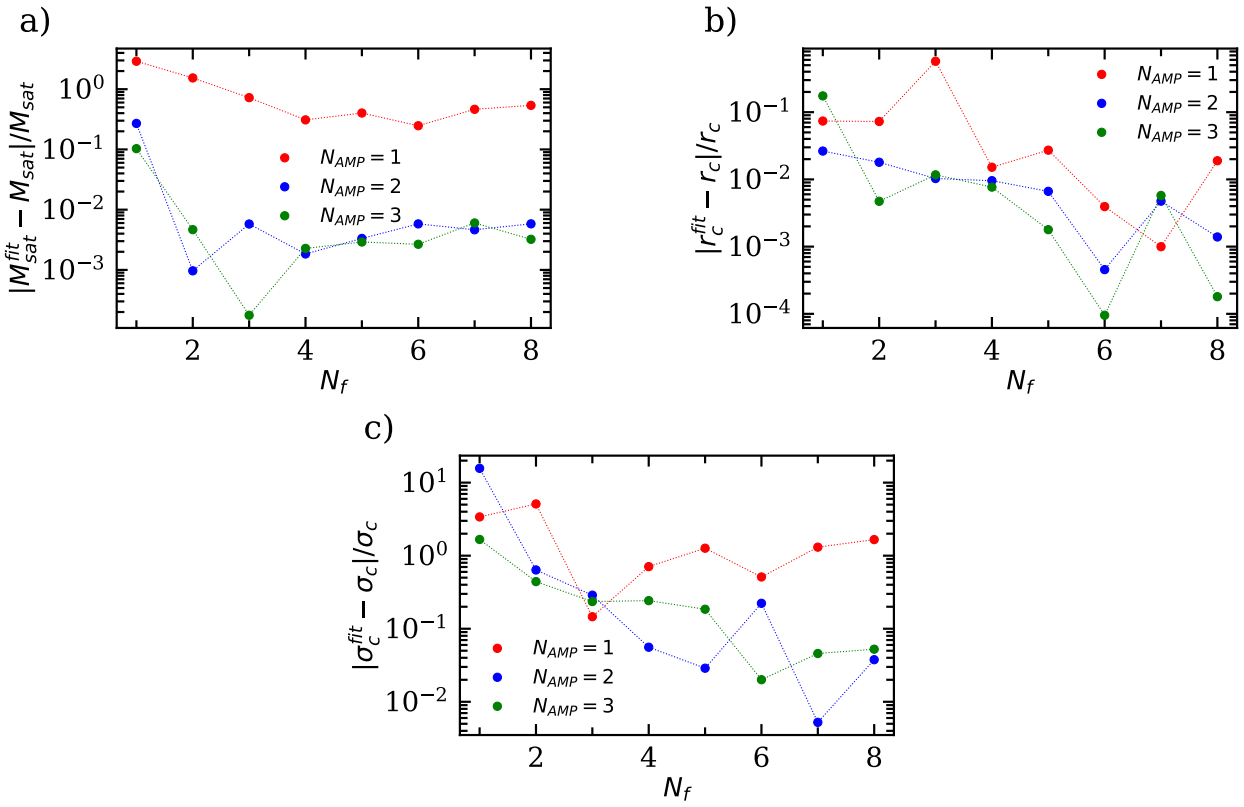

Figure S5: Relative error between the fit and the parameters used in the simulations as a function of the number of measurements used in the fit. Panel (a) shows the fit for M_s, panel (b) for r_c, and panel (c) for σ_c. The parameters used in the simulations are $M_s = 150\,\mathrm{kA/m}$, $r_c = 15\,\mathrm{nm}$, and $\sigma_c = 0.1 \cdot r_c$.

In this section, we analyze how the relative errors between the fits and the simulation values vary depending on the number of frequencies, N_f, and the number of amplitudes, N_{AMP}, used in the fitting process. The maximum number of frequencies and amplitudes considered corresponds to those employed throughout the rest of this work: $H_0 = 4$, 12, and 24 kA/m, and $f = 10$, 20, 30, 40, 50, 60, 80, 100 kHz. When reducing the number of field amplitudes, we first removed the 4 kA/m amplitude, followed by the 12 kA/m. To reduce the number of frequencies, we eliminated them in descending order, starting with the highest.

Figure S5 illustrates how the relative error varies as a function of N_f for different values of N_{AMP}. In all three cases studied, we observe that using at least two field amplitudes is

essential to achieve accurate parameter estimations. For fitting M_s, two field amplitudes and two or three frequencies are sufficient. However, for accurately fitting σ_c, it is necessary to employ a larger number of frequencies (at least six).

SQUID measures of the MNPs

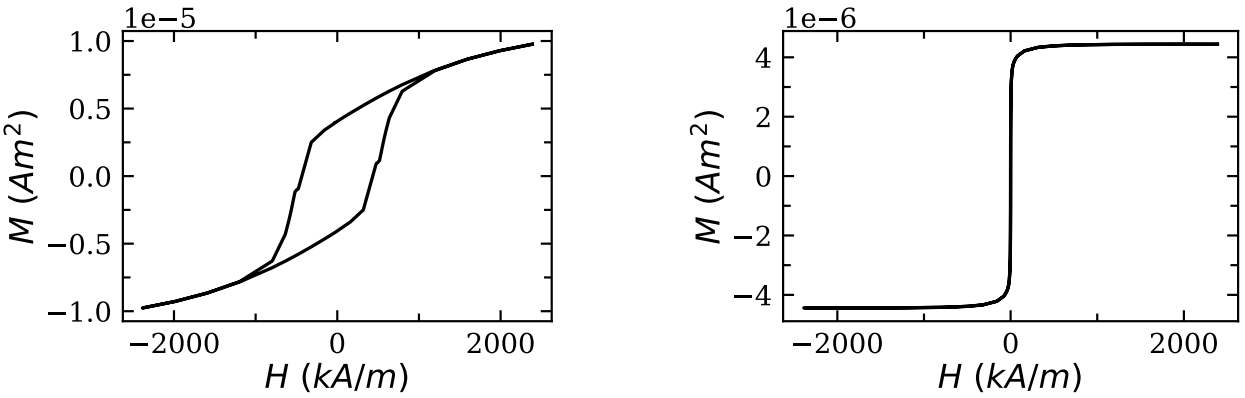

(a) T = 4K

(b) T = 298 K

Figure S6: DC magnetization cycles of the particles measured using a SQUID device at a) 4K and b) 298 K.

In figure S6 we show the DC magnetization of the particles at 4K and 298K. From the cycle at 4K we note that the coercive field is very large which indicates the anisotropy constant is big enough to consider the particles ferromagnets.

TEM images of the MNPs

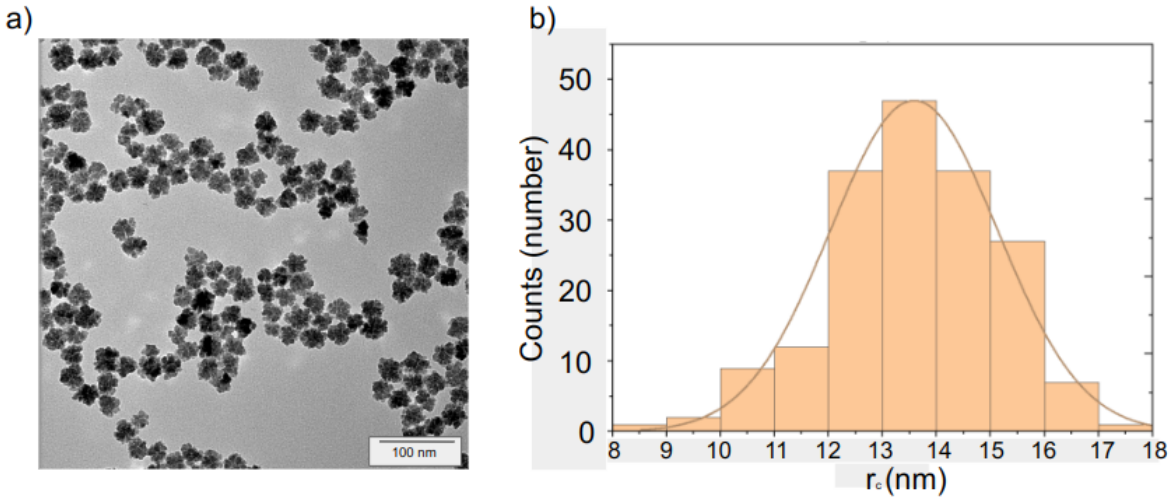

Figure S7: a) TEM image of the MNPs employed in the experiments. b) Histogram of the radius of the core of the particles. The mean radius is 13.58 nm and the standard deviation is 1.55 nm